Available online at www.sciencedirect.com
SCIENCE DIRECT®
International Journal of Multiphase Flow 31 (2005) 1049–1058
International Journal of Multiphase Flow
www.elsevier.com/locate/ijmulflow

Brief communication

Void fraction invariance properties of condensation flow inside a capillary glass tube

Béatrice Médéric *, Pascal Lavieille, Marc Miscevic

Laboratoire d' Energétique—118, route de Narbonne 31062, Toulouse Cedex 4, France

Received 24 March 2005; received in revised form 1 June 2005

1. Introduction

The void fraction is an important parameter for two-phase flow characterization. It is usually determined by means of correlations (e.g. Zivi, 1964; Rouhani and Axelsson, 1970; Chisholm, 1972) which have all been validated using experimental data for pipes with diameters next to 1 cm. In addition, the calculations generally prevent the shear stress modeling from being taken into account. Correlations are widely used because they do not require the phase velocities to be known. For narrow pipes, the heat fluxes involved are small and instrumenting the test section to measure the fluxes is a tough task due to the small scale. Moreover, at this scale, the vapor and liquid distribution is modified because of the change in the relative influence of gravity, viscous and surface tension forces. So, the validity of these correlations remains questionable for flows within capillary tubes. More detailed models have to be developed requiring the knowledge of a local parameter (e.g. void fraction). One way to determine the void fraction profile consists in using non-intrusive methods, such as direct visualization.

Triplett et al. (1999) were interested in the experimental determination of this parameter in air–water flow between 1.1 and 1.45 mm inner diameter pipes for different flow regimes. They compared their experimental values with the equivalent homogeneous fluid model and correlations (Zivi, 1964; Rouhani and Axelsson, 1970). For an annular regime, all approaches overpredict experimental data. For bubbly and slug regimes, the equivalent homogeneous fluid model gives the best predictions.

* Corresponding author. Tel.: +33 561556216; fax: +33 561556021.
E-mail address: mederic@energetique.ups-tlse.fr (B. Médéric).

0301-9322/$ - see front matter
doi:10.1016/j.ijmultiphaseflow.2005.06.004

Non-intrusive methods have already been developed in the case of large diameter channels. For instance, Wojtan et al. (2005) investigated the experimental determination of the void fraction for a boiling stratified flow for mass fluxes ranging from 100 to 150 kg/(m^2 s). The test section was lit by means of a laser sheet allowing a precise determination of the liquid–vapor interface shape. They compared their experimental values with the equivalent homogeneous fluid model and the correlations of Zivi (1964), Taitel and Dukler (1976) and Rouhani and Axelsson (1970). The smallest deviation is given by the model of Rouhani (<10%).

In this paper, we present the determination of the local void fraction profile for a condensation flow within a capillary tube of internal diameter 0.56 mm. We used direct visualization (i.e. ombroscopy). First of all, the experimental setup allowing the study of convective condensation will be introduced. As the cylindrical geometry of the tube induces a distortion in the liquid–vapor interface shape, an optical model used for the correction of film thickness determination was employed. The time averaged void fraction profiles were then drawn for different flow regimes established according to the mass flow rate. The invariance properties of these profiles are highlighted. Finally, the void fraction, averaged according to the condensation length, is presented as a function of the flow regimes.

2. Experimental setup

The experimental setup (Fig. 1) is made up of a syringe-pump, a glass syringe, an evaporator, the test section and an outlet tank. The round borosilicate glass tube had an inner diameter of 0.56 mm and a length of 100 mm. Twenty milliliters of *n*-pentane in the liquid state was stored in the syringe. The syringe-pump was used to push the pentane with a constant mass flux in

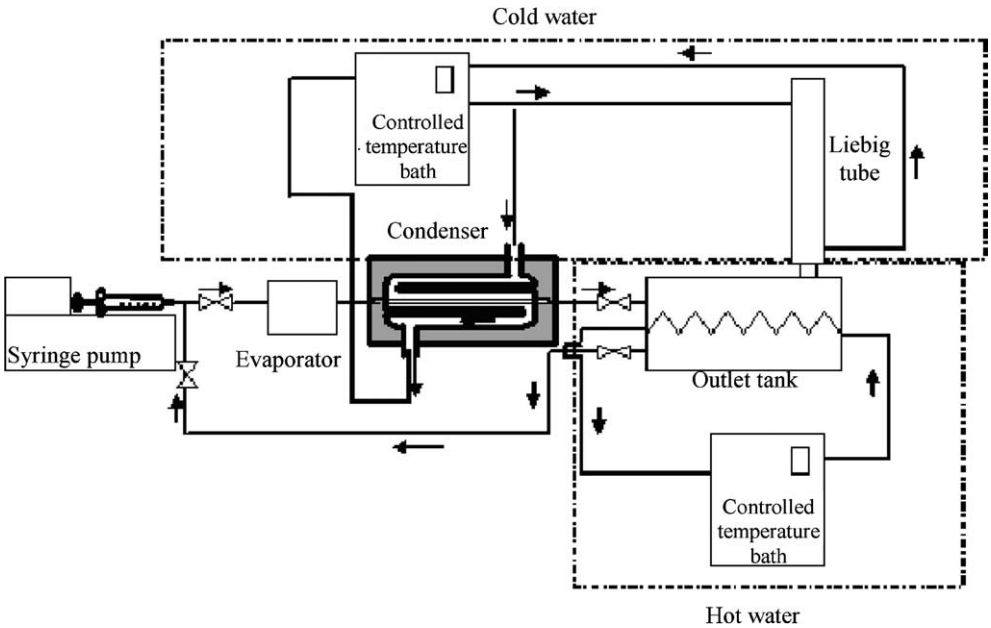

Fig. 1. Photograph of the experimental setup.

the test section, in the range 0–18 kg/(m^2 s). The experimental conditions were chosen to get complete condensation in the visible zone of the capillary glass tube. The flow rate accuracy was 0.07 kg/(m^2 s). The liquid was then vaporized in the evaporator zone i.e. a 70 mm length cylindrical stainless steel tank. Heating was from an electrical resistance. To reduce heat losses, the evaporator was wrapped with glass wool. The fluid temperature at the evaporator outlet was fixed at 40 °C. As the saturation temperature of the pentane is near 36 °C, the vapor is slightly overheated. Complete convective condensation of the vapor was achieved in the test section which was cooled by circulating water at 10 °C. The condensate was sent to the outlet tank at atmospheric pressure. To visualize the flow in the steady state, the test section was lit with a stroboscope and the images recorded by means of a CCD camera at a rate of 25 frames per second. The acquisition window was 4.5 mm long and recording lasted 40 s. The CCD camera was on a moving plate controlled by two micrometric screws. Images were thus obtained over the whole condensation length by moving the camera 4 mm at each step.

3. Optical method

3.1. Ray trajectory

The optical model developed assumes a two-dimensional pattern. Condensation occurs on the tube wall; the liquid remains at the periphery, and the vapor in the core of the channel due to the relatively slight effect of gravity.

Considering these hypotheses, an axisymmetric liquid film with a given thickness δ settles inside the pipe (Fig. 2). All the heat exchanger dimensions and the camera lenses characteristics are taken

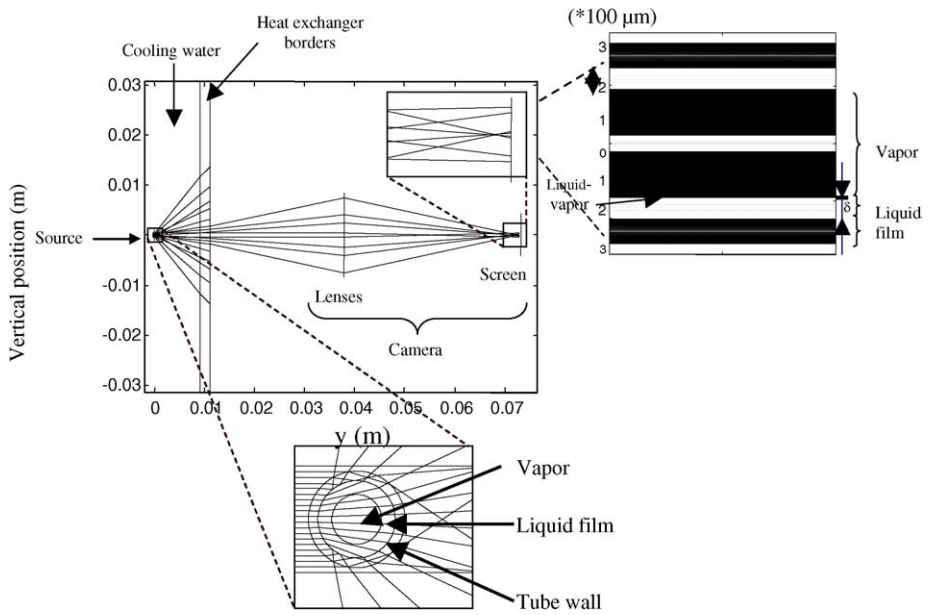

Fig. 2. Example of ray propagation from the source to the receiver, and of the reconstructed image on the camera receiver.

into account. The stroboscope light is represented here by a parallel source of 10 000 rays uniformly distributed over the whole height of the pipe. This number can be increased for more local analysis, notably for very thin liquid films. Ray propagation from the source to the camera follows the laws of optical geometry (Descartes laws). The ray trajectory is broken down into a succession of points, between which light propagation is straight. Indeed, the refractive index is considered to be homogeneous in each medium. Fig. 2 gives the main stages for determining the path of the ray from the source to the receiver (if its path allows this destination to be reached).

The aim of the first part of this study is to determine the successive impact points of the ray with the different cylindrical interfaces. In order to prevent an infinite succession of complete refractions, the program stops calculating the ray's path when its length is twice that of the outer pipe diameter. If the ray goes out of the pipe, it is then extended up to the external wall of the heat exchanger by taking into account the index variations while it crosses both straight interfaces encountered at the heat exchanger glass borders. Then, if the direction of the ray at the exit of the exchanger allows the lenses to be reached, the impact point with the first lens is determined. So the Gauss approximation is used to obtain the new ray direction at the lens exit. Finally, the impact point on the CCD receiver can be determined. So, the number of rays received by each CCD sensor is converted into a grey level. The calculation is then iterated for all the source's rays, and for all the geometric shapes (various film thicknesses, screen positions, etc.).

The whole picture given by the camera for a constant film thickness may be reconstructed. Fig. 2(right) represents the picture that the camera would acquire for a liquid film thickness of 90 μm. The light zone located around $y = 0$ corresponds to the rays which arrive on the cylindrical wall with an impact close to normal. Their paths are only slightly changed generating a very light band in the center of the pipe.

The light zones located around $y \approx 200$ μm and $y \approx -200$ μm represent the liquid film whose thickness is equal to 90 μm. On the reconstructed picture, this thickness is found to be equal to 64 μm which represents a deviation of about 30%. It is particularly interesting to note that the liquid–vapor interface is materialized by extreme brightness variations. The interface position can thus be discerned unambiguously whatever the threshold chosen during the image digitalization process.

3.2. Calibration curve

As illustrated above, the cylindrical pipe geometry deforms the picture acquired by the camera. In the case of condensation in the pipe, it may considerably change the evaluation of film thickness. A calibration curve is also needed to obtain the true film thickness from the one measured from the picture.

To obtain the calibration curve, the same procedure as the one described in Section 3.1 was applied for imposed film thicknesses varying from 0 to 280 μm in steps of 5 μm. The calibration curve (Fig. 3) obtained gives the correspondence between the thickness seen by the camera (δ_{seen}) and the real film thickness (δ_{real}). The curve also indicates the smallest film thickness measurable due to the camera's limits. First of all, image processing cannot differentiate films less than 12 μm thick. The rays which cross such thin films are strongly deviated and do not reach the camera lens (Fig. 3).

For values between 18 and 25 μm, the film thicknesses acquired on the camera are quite unchanged, close to 5 μm, due to the astigmatism induced by the deformation. The processing

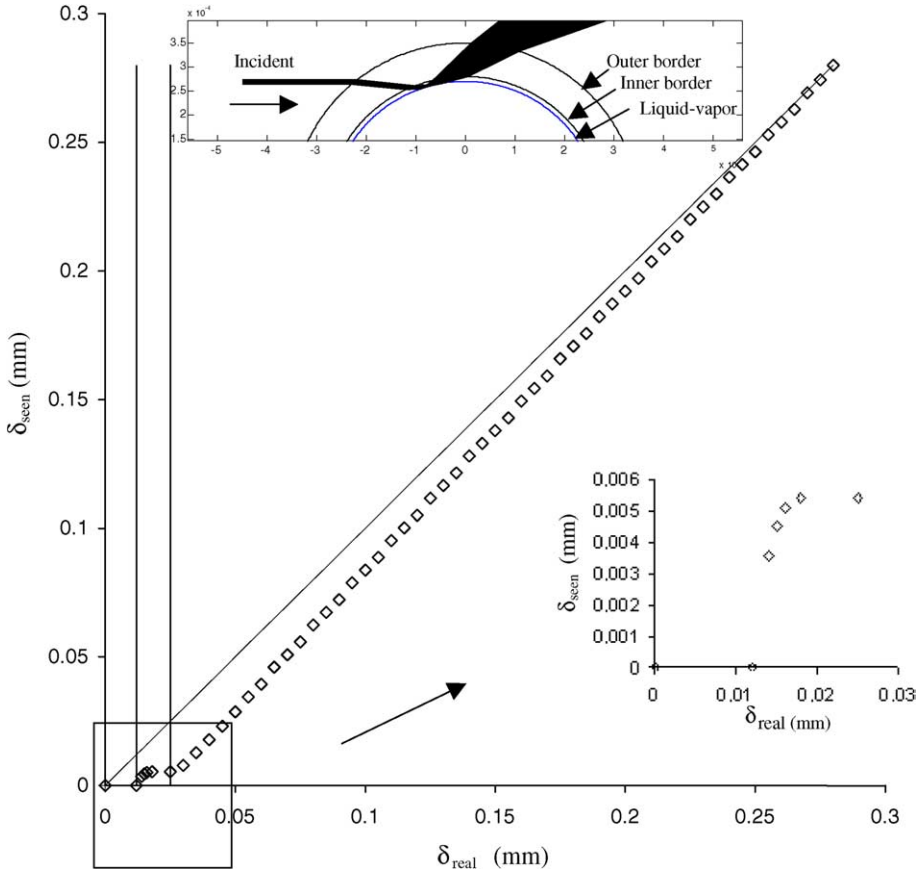

Fig. 3. Calibration curve obtained by simulation, representing the liquid film thickness seen on the camera as a function of the imposed thickness of the liquid film in a 0.56 mm inner diameter tube.

becomes more accurate beyond 25 μm; the deviation diminishes as the film thickness increases. Nevertheless, the liquid film thickness obtained with the camera has to be corrected whatever its value. As an example, for a true thickness of 30 μm, the value acquired by the camera is 7 μm. This difference could represent a mistake of more than 300% if the thickness measured on the picture is considered as being the true one.

The pipe seen in the acquisition window was then divided into 280 cross-sections each with a length of 1 pixel (≈16 μm). For each section, the thickness of the liquid film is determined. Using the calibration curve, the observed thickness is converted into a ''real'' thickness. The axial variation of the ''real'' liquid thickness is thus determined.

4. Flow regimes and associated void fraction axial shapes

The range of mass fluxes under study leads to four condensation regimes. The description may be found in detail in Médéric (2004).

From the measurement of the film thickness δ, the value of the void fraction may be determined. Applying the hypothesis of an axisymmetric flow structure, the void fraction α is given by relation (1):

$$\alpha = \left(1 - \frac{2\delta_{\text{real}}}{D}\right)^2, \tag{1}$$

where D is the inner diameter of the capillary tube.

The film thickness uncertainty is equal to 1 pixel (16 μm). However, this value is strongly reduced considering the average of 1025 pictures and the uncertainty considering the time averaged film thickness falls to a value less to 1 μm.

An example of the instantaneous void fraction profile is shown in Fig. 4c. This void fraction shape corresponds to the flow structure represented in Fig. 4a.

The annular zone prevails between 0 and 0.4 mm. In this zone, the very thin film is not discernable by the image processing ($\delta < 12$ μm). Then, a liquid slug is formed which decreases the void fraction to 0.2. The formation of the Taylor bubble which reaches the pipe wall leads to a value of the void fraction equal to 1. The zone completely filled with liquid between 2.9 and 3.2 mm has a

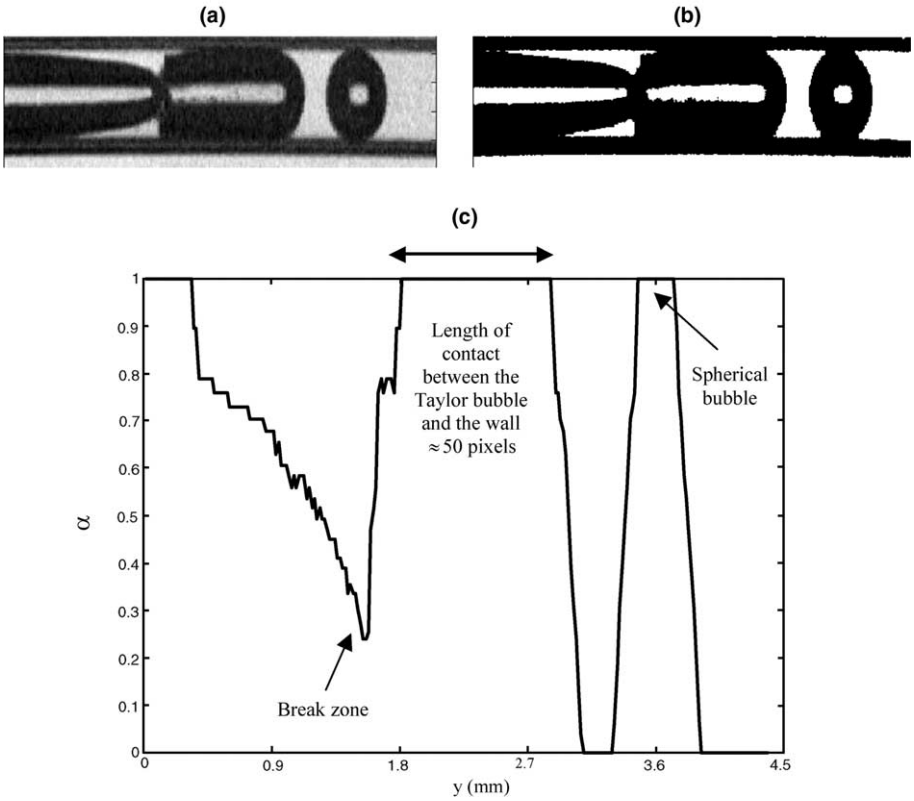

Fig. 4. (a) Example of image obtained with the camera for a mass flux value G of 11.35 kg/(m^2 s). (b) Same image obtained after digitalization. (c) Instantaneous void fraction profile deduced from digitalized image as a function of the longitudinal position.

void fraction of 0. This value returns to 1 because of the spherical shape of the next bubble which occupies the whole cross-section.

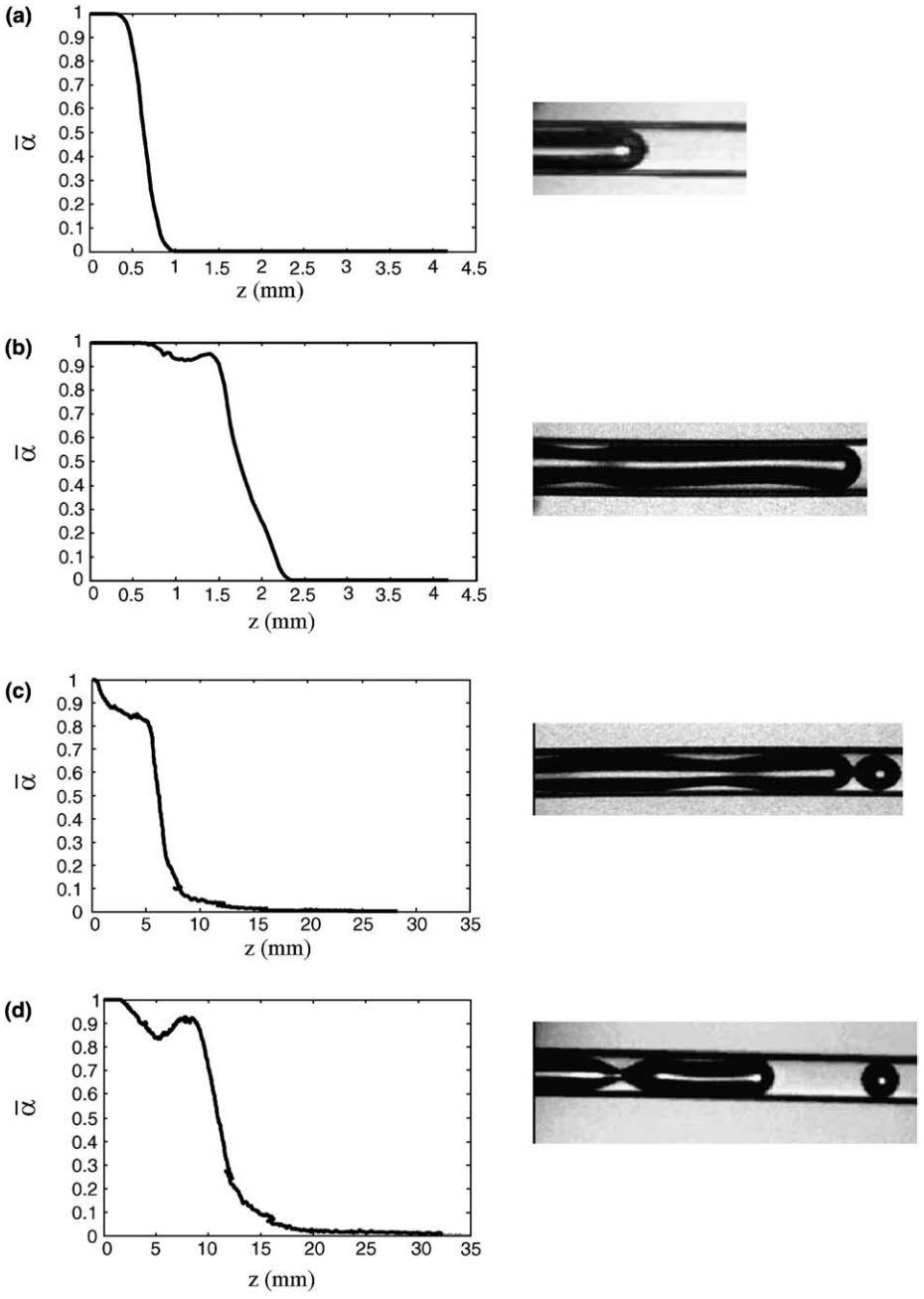

Fig. 5. Void fraction profiles according to the flow structures observed (a) capillary flow ($G = 3.4$ kg/(m^2 s)), (b) annular wavy flow ($G = 4.8$ kg/(m^2 s)), (c) annular with spherical bubble ($G = 8.9$ kg/(m^2 s)), (d) annular with Taylor and spherical bubbles ($G = 13.8$ kg/(m^2 s)).

Note that void fractions recorded as being equal to 1 present a non-negligible uncertainty. Indeed, as the thinnest film that can be measured is 12 μm thick, instantaneous local void fractions greater than 0.916 lead to a value of 1. Here, the void fraction profiles are averaged considering the 1025 pictures contained in the sequence acquired with the camera. The resulting uncertainty remains small with a value of less than 1%. The results are reported in Fig. 5 according to the type of flow regime observed in the test section.

The profile of average void fraction α retranscribes the condensation flow structures observed. In the case of an annular (or capillary) regime, the void fraction is almost equal to 1. Then, it falls rapidly to 0 along the curvature of the meniscus (Fig. 5a). In the case of an annular wavy flow (Fig. 5b), the void fraction is close to 1 in the entry region. However, the presence of a wave along the liquid–vapor interface makes its value fall to 0.9. For these two regimes, the condensation lengths are short (few millimeters). For the regime introducing the release of spherical bubbles (Fig. 5c), the condensation zone length increases drastically (few centimeters). In the entrance region, the void fraction diminishes towards values ranging between 0.9 and 0.8. This is due to the presence of unstationary waves. In contrast, once spherical bubbles are formed, the void fraction strongly decreases. In the case of a regime with elongated bubbles (Fig. 5d), the behavior differs. Indeed, a greater rise of the void fraction appears after the end of the annular zone. It corresponds to the formation, predominantly in this zone, of the elongated bubble. Then, the void fraction decreases sharply corresponding to the beginning of the bubbly zone.

Void fraction profiles, as a function of the non-dimensional axial position y/L_d (where L_d is the condensation length) are represented in Fig. 6 considering different values of mass flux. The values 3.4 and 4.8 kg/(m^2 s) correspond to capillary regime while the mass fluxes equal to 8.9 and 13.8 kg/(m^2 s) lead to regimes with formation of bubbles. This representation exhibits a nearly

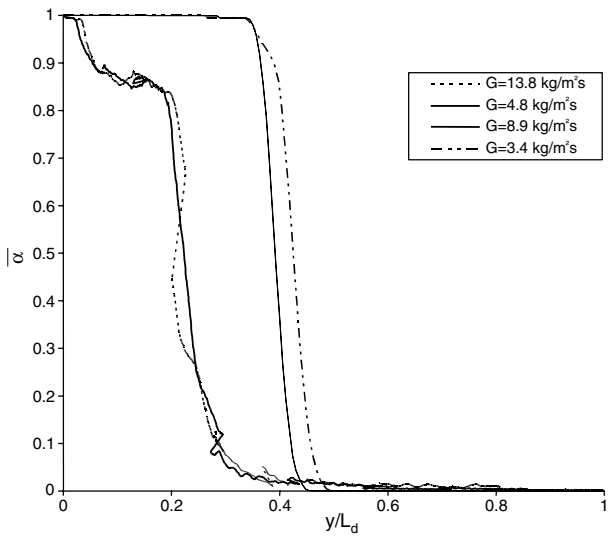

Fig. 6. Time averaged void fraction $\bar{\alpha}$ versus the non-dimensional axial position (y/L_d). L_d represents the length of the condensation zone.

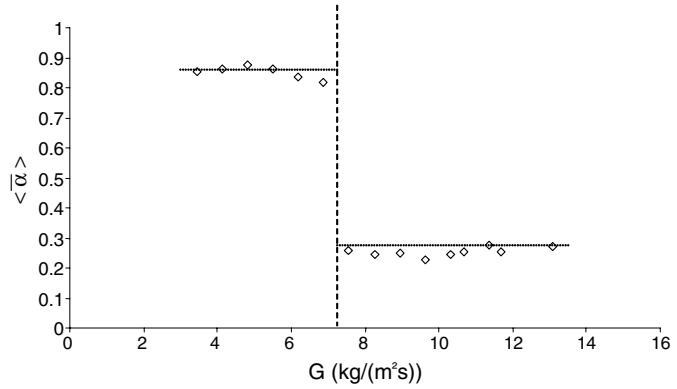

Fig. 7. Mean void fraction $\langle\bar{\alpha}\rangle$ in the two-phase zone as a function of the mass flux G.

constant profile according to the regime considered and the homothetic nature of the local void fraction variation along the two-phase zone.

5. Average void fraction

To illustrate this invariance property of the void fraction profile according to the flow structure, let us consider the mean void fraction defined as (2):

$$\langle\bar{\alpha}\rangle = \frac{1}{L_d}\int_0^{L_d} \bar{\alpha}(z)\mathrm{d}z. \tag{2}$$

The void fraction profile and the condensation length being known for each of the regimes encountered, these values may be easily determined and are reported in Fig. 7.

The results reveal a threshold which delimits two behaviors: for low mass flux values, the mean void fraction is nearly constant around 0.85. This behavior corresponds to the annular regime. For higher mass fluxes, i.e. for regimes involving the formation of bubbles, the mean void fraction falls to 0.25. The decrease of the average void fraction corresponds to the abrupt increase of condensation length caused by the appearance of a bubbly zone in which the rate of phase change is small.

6. Conclusions

A specific experimental setup has been designed to visualize the condensation flow inside a capillary tube. The transparency of the condenser allows the visualization of four condensation regimes for the range of mass fluxes considered. Thanks to image editing, it is possible to get the instantaneous or time averaged void fraction profiles as a function of the axial position. Moreover, the time averaged void fraction as a function of the non-dimensional axial position reveals a particular type of profile according to the flow structure considered. As a consequence, the mean void fraction in the two-phase zone reveals two major flow structures: a regime with a high void

fraction equal to 0.85 and regimes presenting a release of bubbles with void fraction equal to 0.25. It appears that mean void fraction should be considered as constant for a given flow structure whatever the value of the mass flux considered in the present study.

References

Chisholm, D., 1972. An equation for velocity ratio in two-phase flow. NEL report, Scotland.

Médéric, B., 2004. Etude de la condensation convective en mini-tube: analyse des instabilités. Ph.D. Thesis, Université Paul Sabatier, Toulouse, France.

Rouhani, Z., Axelsson, E., 1970. Calculation of void volume fraction in the subcooled and quality boiling regions. International Journal of Heat and Mass Transfer 13, 383–393.

Taitel, Y., Dukler, A.E., 1976. A model for predicting flow regime transitions in horizontal and near horizontal gas–liquid flow. AIChE Journal 22, 43–55.

Triplett, K.A., Ghiaasiaan, S.M., Abdel-Khalik, S.I., LeMouel, A., McCord, B.N., 1999. Gas–liquid two-phase flow in microchannels Part II: void fraction and pressure drop. International Journal of Multiphase Flow 25, 395–410.

Wojtan, L., Ursenbacher, T., Thome, J.R., 2005. Measurement of dynamic void fractions in stratified types of flow. Experimental Thermal and Fluid Science 29, 383–392.

Zivi, S.M., 1964. Estimation of steady state void fraction by means of minimum entropy production. Journal of Heat Transfer 86, 247–252.